Journal of Ceramic Processing Research. Vol. 21, Special. 1, pp. s1~s8 (2020)
(Received 11 December 2019, Received in revised form 17 March 2020, Accepted 20 March 2020)
https://doi.org/10.36410/jcpr.2020.21.S1.s1

J O U R N A L O F
Ceramic Processing Research

Tunable ternary doping effect of protein-based carbon derived from tofu for energy storage devices

Hyun-Gi Jo[a], Geon-Hyoung An[b] and Hyo-Jin Ahn[a,b,*]
[a]*Department of Materials Science and Engineering, Seoul National University of Science and Technology, Seoul 01811, Korea*
[b]*Program of Materials Science & Engineering, Convergence Institute of Biomedical Engineering and Biomaterials, Seoul National University of Science and Technology, Seoul 01811, Korea*

Carbon used as an electrode material for lithium ion batteries (LIBs) is being continually developed to improve its electrochemical performance and lower its cost. Recently, many attempts to achieve high capacity and high-rate cycling stability in carbon materials have been made. However, carbon materials still face major problems, such as limited raw material resources, a high temperature process, and a complex synthesis method. Herein, to solve these problems, we report an approach to synthesizing tunable ternary (boron, phosphorus, and nitrogen)-doped carbon derived from tofu using a simple doping process. Tunable ternary-doped carbon materials, which show a synergistic effect when used with protein-based tofu, including N and the introduced heteroatoms (B and P), are successfully synthesized. The tunable ternary doped carbon materials showed improved specific capacity (381 mAh g^{-1} after 100 cycles at 100 mA g^{-1}) and excellent high-rate cycling stability (190 mAh g^{-1} after 400 cycles at 2000 mA g^{-1}). These results were attributed to the synergetic effect of enhanced carbon conductivity from B-doping, increased functional groups from P-doping, and an increase in the number of active sites from N-doping. Therefore, tunable ternary-doped carbon materials derived from tofu may be used as a potential electrode for high-performance LIBs.

Keywords: Lithium ion batteries, Carbon, Heteroatom doping, Synergistic effect, High-rate performance.

Introduction

Lithium ion batteries (LIBs), which are mainly used in portable electronic devices such as smart phones, laptops, and tablet PCs, are eco-friendly energy storage devices due to their high energy density (theoretical specific capacity of 372 mAh g^{-1}) and cycle stability (80% of the original capacity after 300 cycles) compared with other commercial rechargeable batteries [1]. Recently, studies on LIBs for application in electric vehicles (EVs) have been actively studied [2, 3]. However, despite various efforts, the performance improvement in LIBs for EVs has not yet met requirements. For example, for use in practical EVs, the relevant technologies still require an anode, a cathode, an electrolyte, and a current collector. Synthetic graphite fabricated from the heat treatment of pith or coke at a high temperature (above 1,000 °C) is currently used as a commercial anode [4]. However, for synthetic graphite, problems such as limited raw materials, complex processes, high production cost, and high-temperature synthesis have still not been solved.

Recently, various bio-materials such as crops, including the seeds and shells of plants, and nutrients, including carbohydrates and sugars (glucose, starch, and cellulose), have been used as a carbon-based anode replacement for synthetic graphite [5-11]. They have attracted considerable attention because they are plentiful natural resources, and the cost of manufacturing with these materials is low. Tofu, which is made from soybean, has also been used as bio-material. Tofu is composed of protein, fat, and water. Furthermore, tofu consisting of amino acid-based protein can be carbonized in an inert gas [12-15].

Recently, to improve the performance of energy storage devices including LIBs, strategies such as heteroatom doping, plasma treatment, and nano-structured composition have been tried [16-18]. Of these strategies, heteroatom doping has received considerable attention for use in LIBs due to its resulting high energy density and excellent cycle stability. For example, Bulusheva et al. synthesized multi-walled nitrogen-doped carbon (CN_x) nanotubes using an aerosol-assistanted catalytic chemical vapor deposition technique, together with 270 mAh g^{-1} at a current density of 0.2 mA cm^{-2} [19]. Zhang et al. synthesized phosphorus-doped graphene through thermal annealing and the triphenylphosphine (TPP) method, which was observed to be 460 mAh g^{-1} at a current density of 0.1 mA g^{-1} [20]. Despite these efforts, further study to enhance electrochemical performance by using ternary doping in LIBs remains a critical issue.

In this study, we performed tunable ternary doping of

*Corresponding author:
Tel : +82-2-970-6622
Fax: +82-2-973-6657
E-mail: hjahn@seoultech.ac.kr

protein-based carbon derived from tofu for LIBs using carbonization. Heteroatom doping of carbon derived from tofu can be an effective preparation for a LIB anode. It can also overcome the critical problems of carbon-based materials with its environmental friendliness, simple manufacturing process, high energy density, and excellent cycle stability. Also, additional heteroatoms, including B and P, were used to improve conductivity along with the carbon, and to enhance the functional groups on the carbon surface.

Experiments

The tofu used to fabricate the carbon was purchased from Pulmuone Co., Ltd. (Korea). The tofu was stirred with phosphorus red (P_4, Aladdin, 98.5%) for 2 h. After the tofu was mixed with phosphorus red, it was dried in an oven at 80 °C until any moisture was removed, and then stabilized at 400 °C in air. The stabilized tofu was acid-treated using nitric acid (HNO_3, Junsei, 66%) to remove impurities. The tofu with impurities removed was ball-milled by adding boric acid (H_3BO_3, Aldrich, 99.99%). Carbonization was performed at 800 °C under a nitrogen atmosphere. Finally, four different types of samples were produced, and are referred to as N-doped C, B@N-doped C, P@N-doped C, and B@P@N-doped C.

The structures and morphologies of the samples were characterized by field-scanning electron microscopy (FESEM, Hitachi S-4800) and transmission electron microscopy (TEM, MULTI/TEM; Tecnai G^2) with energy-dispersive X-ray spectrometry (TEM-EDS mapping, Philips CM20T/STEM). To demonstrate the contents, thermogravimetric analysis (TGA) in a temperature range of 200 to 900 °C at a heating rate of 10 °C min^{-1} in air was performed. The crystal structures and

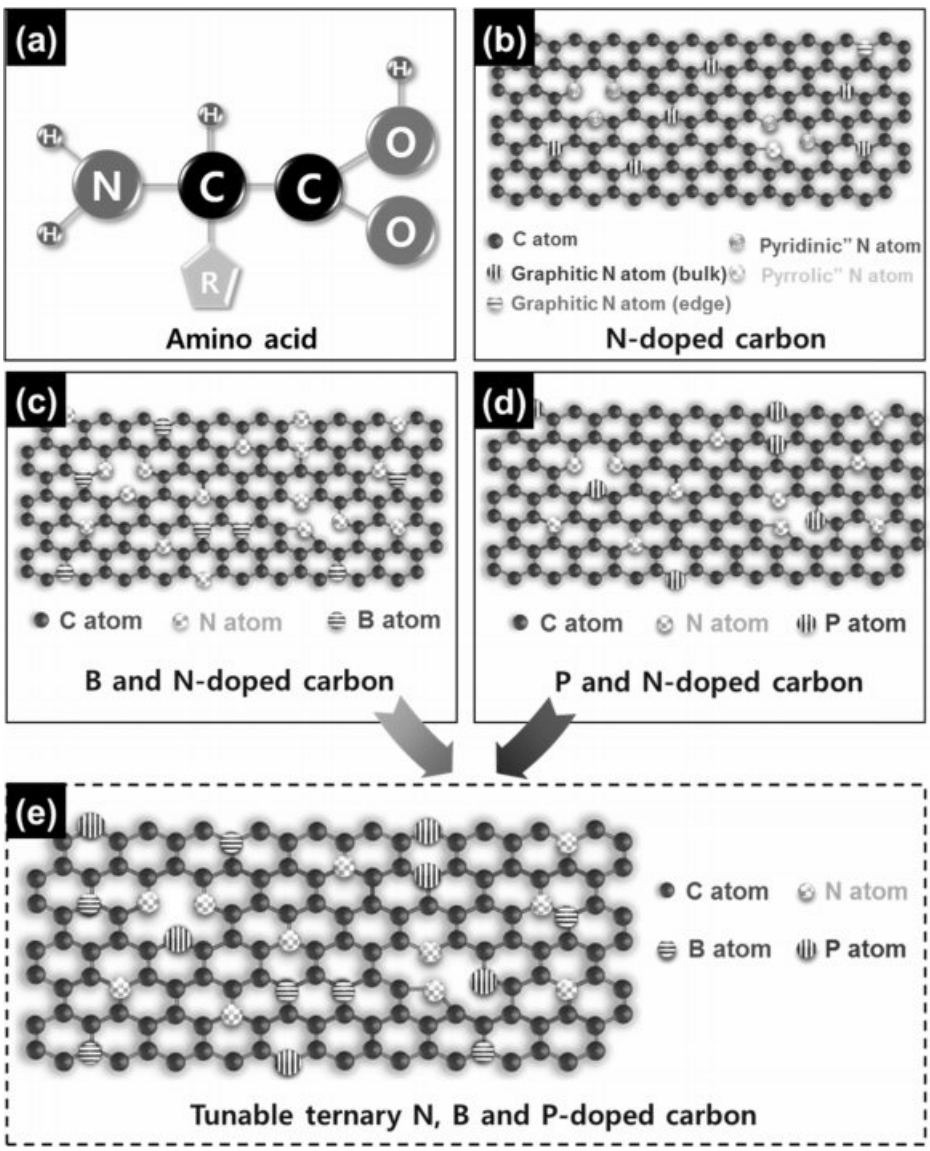

Fig. 1. Schematic illustration of N, B, and P doping system in the carbon lattice structure.

chemical bonding states of the samples were examined by X-ray diffractometry (XRD, Rigaku D/Max-2500 diffractometer using Cu K_a radiation) in the range of 10° to 90° with a step size of 0.02° and X-ray photoelectron spectroscopy (XPS, ESCALAB 250 equipped with an Al K_a X-ray source), respectively. All electrochemical measurement tests were performed using coin cells (CR2032, Hohsen Corporation), which consisted of tunable ternary doped carbon materials as the anode, Li metal foil (Honjo Chemical, 99.8%) as the cathode, a porous polypropylene membrane (Celgard 2400) as the separator, and a 1.0 M $LiPF_6$ solution in a mixture of ethylene carbonate and dimethyl carbonate (1:1) as the electrolyte. The ternary-doped carbon materials were fabricated from a paste slurry with a mixture of active materials (70 wt%), PVDF (20 wt%) as the binder, and Ketjen black (10 wt%) as the conducting material. These were dissolved in N-methyl-2-pyrrolidinone solvent (NMP, Aldrich), and the paste slurry was coated on a Cu foil substrate (Nippon Foil, 18 mm) as the current collector. The prepared electrodes were dried in an oven at 100 ºC for 12 h. All coin cells were assembled in a high-purity argon-filled glove box. To investigate the electrochemical kinetics of the prepared electrodes, electrochemical impedance spectroscopy (EIS) measurements were performed in the frequency range of 10^5 to 10^{-2} Hz by using an AC signal of 5 mV. The discharge-charge tests were performed using a battery cycler system (WonATech Corp., WMPG 3000) in the potential range of 0.0–3.0 V (versus Li/Li^+) at 25 ºC in an incubator. The cycling stability was investigated for up to 100 cycles at a current density of 100 mA g^{-1}. The high-rate cycling performance was measured at current densities of 100, 300, 500, 700, 1,000, and 2,000 mA g^{-1}. The ultrafast performance of the samples was measured for up to 400 cycles at current densities of 2,000 mA g^{-1}.

Results and Discussion

Fig. 1 shows a schematic illustration of amino acids, N-doped carbon, B and N-doped carbon, P and N-doped carbon, and tunable ternary (B, P, and N)-doped carbon. The amino acids, as a component of proteins, consist of both amino and carboxyl groups, which can be carbonized to serve as sites for doping elements (Fig. 1a). Carbon derived from tofu was made into N-doped carbon due to the nitrogen in the amino acid [13, 21]. The N-doped carbon produced during the carbonization process has a graphite lattice structure [22]. In particular, the N atoms have three different arrangements, depending on their doping positions (Fig. 1b). Specifically, they are classified as graphite-N when located on the bulk or edge in the carbon lattice plane, as pyridine-N atoms when bonded to two C atoms in the formation of one π electron, and as pyrrolic-N atoms when combined with two C atoms located in the heterocyclic ring of the carbon lattice plane [23]. In the case of graphitic-N, they are situated by replacing the C atom with the N atom in the carbon lattice plane. Moreover, the electronegativity of the N atom (3.04) is higher than that of the C atom (2.55), so the N atom can locally control the electronic properties of the carbon lattice plane [24, 25]. The B atoms are present in the C sp^2 frame of three different B-C groups (BC_3, BCO_2, and BC_2O), and the B-O bonds are formed by an electron state transformation at the edges of the carbon lattice structure [26, 27]. In addition, the B atoms induce the electron density state of the C atoms, causing a transition in the electronic structure (Fig. 1c). Finally, the P atoms in the carbon lattice plane represent the four structures of the P-C groups (PCO_2, PCO_3, PC_2O, and PC_2O_2). In general, when the P atoms replace the two edge carbon atoms, oxygen-containing functional groups (-OH, -O, and =O) are formed in the carbon lattice structure [28, 29]. The oxygen-containing functional groups can improve electrochemical performance because they facilitate the charge connection by improving the wettability of the electrolyte (Fig. 1d). Thus, tunable ternary-doped carbon exhibits a synergistic doping structure comprised of an improvement in the active sites from N-doping, improved electrical conductivity from B-doping, and an increase in the number of oxygen-containing functional groups from P-doping (Fig. 1e).

Fig. 2(a–d) shows the SEM images obtained from N-doped C, B@N-doped C, P@N-doped C, and B@P@N-doped C. The diameters of the samples were ~371.6–560.3 nm, ~365.5–587.7 nm, ~343.3–552.9 nm, and ~370.6–542.1 nm, respectively. All samples showed a semi-block morphology, and there was no difference in

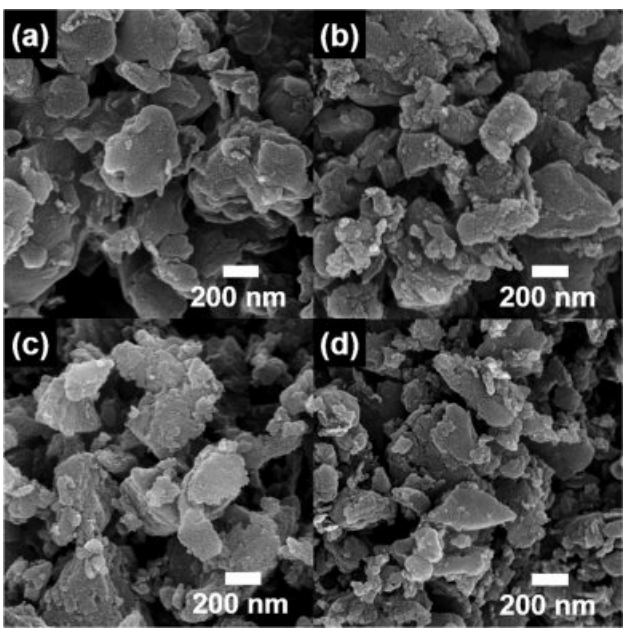

Fig. 2. (a–d) FESEM images of N-doped C, B@N-doped C, P@N-doped C, and B@P@N-doped C.

the particle shape according to the different types of doping elements. To further investigate the structural properties and morphology of the tunable ternary doped carbon, TEM measurements were taken. Fig. 3 exhibits low-resolution (Fig. 3a) and high-resolution (Fig. 3b) TEM images and TEM-EDS mapping (Fig. 3c) obtained from B@P@N-doped C. In Fig. 3(a), the particles can be observed in a semi-block-like structure consisting of various particle sizes. The high-resolution TEM image in Fig. 3(b) indicates that distinct corrugations were also observed on the surface of the B@P@N-doped C. The corrugated surface structure due to the addition of the doping element could be entirely exposed to reactant molecules from the increase in the number of active sites and functional groups (i.e., N, P-doped carbon), and B-doped carbon could improve enhanced carbon conductivity [20, 30]. In Fig. 3(c), to demonstrate the distribution of C, N, B, and P atoms in B@P@N-doped C, TEM-EDS mapping is shown. The EDS results indicate that due to the addition of doping elements, the B and P atoms were uniformly distributed along with the carbon. Also, the N atoms were uniformly dispersed along the carbon due to the N-containing amino acid.

Fig. 4(a) shows the TGA measurements for the content of the samples. The overall graph of all samples exhibited weight loss with an increase in temperature. However, the thermogravimetric reduction starting at around 450 ºC and ending at around 600 ºC shows a slight difference for the different doping

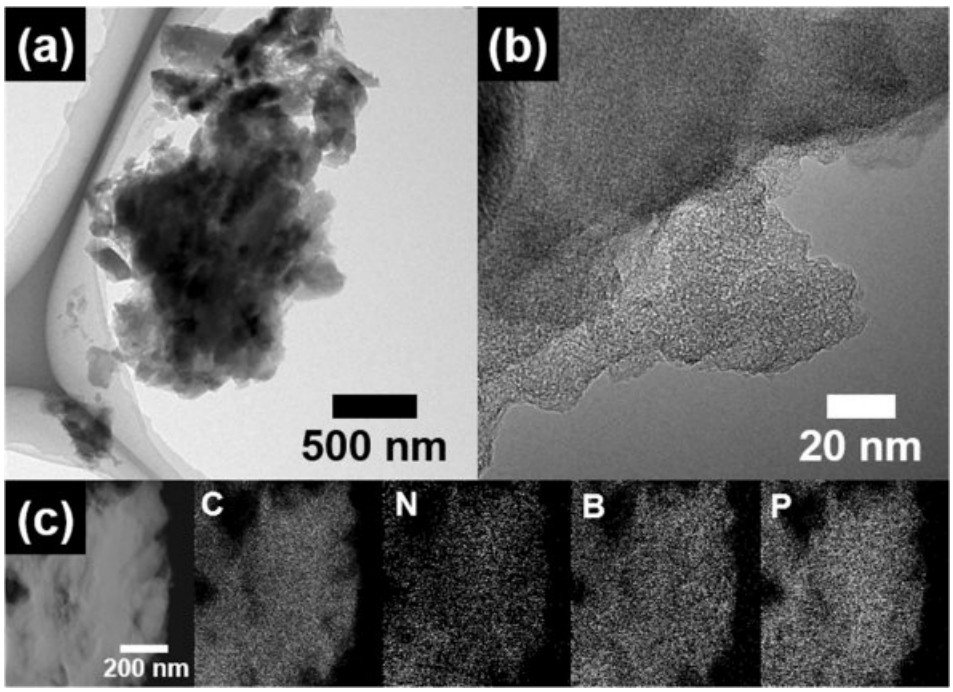

Fig. 3. (a) Low-magnification and (b) high-magnification TEM images, and (c) TEM-EDS mapping result obtained from B@P@N-doped C.

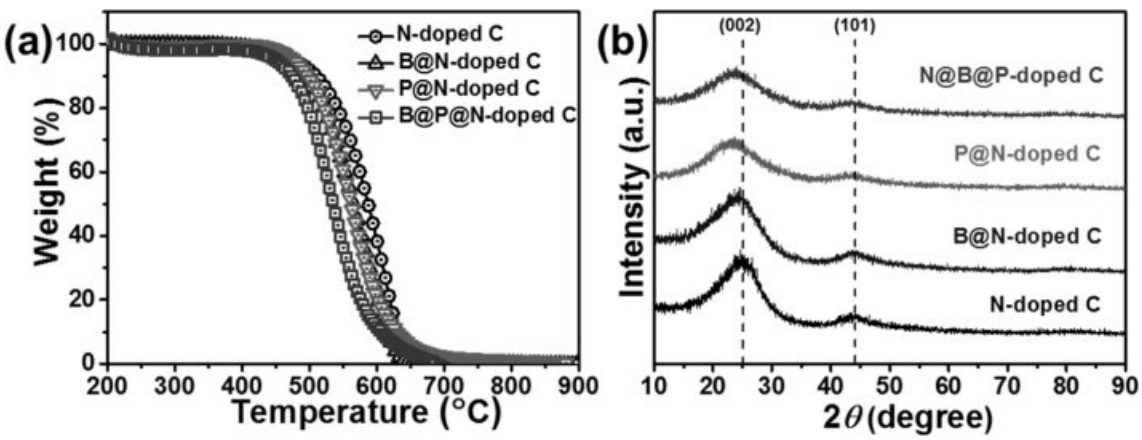

Fig. 4. (a) TGA curves and (b) XRD patterns of N-doped C, B@N-doped C, P@N-doped C, and B@P@N-doped C.

elements. This is because of the difference in atomic structural defects inherent in the bonding of carbon [31]. In particular, B@P@N-doped C shows a weight loss starting at the lowest temperature, due to the increased atomic structural defects. This result implies that tunable ternary-doped carbon derived from tofu can be successfully fabricated by carbonization. Fig. 4(b) shows the XRD patterns of the samples. All samples exhibit wide peaks at approximately 25°, corresponding to the (002) plane of graphite. These peaks show a lower-angle shift in the (002) plane because of the doping effect. The peaks appear at ~25.2° for N-doped C, ~25.0° for B@N-doped C, ~24.8° for P@N-doped C, and ~24.4° for B@P@N-doped C [32]. Therefore, the successful synthesis of carbon doped with B, P, and N elements simultaneously was confirmed by TGA and XRD measurements.

To further confirm the incorporation of heteroatoms into the carbon derived from tofu, the chemical bonding states of the samples were examined by XPS measurements, as shown in Fig. 5. The decomposition of the C1s spectra of all samples (Fig. 5a-d) shows four peaks of C-C groups at ~284.5 eV, C-N groups at ~285.3 eV, C-O groups at ~286.6 eV, and N=C-O groups at ~289.0 eV, respectively [33]. Fig. 5(e-h) shows N 1s peaks in the XPS spectra, and the decomposition of N can be observed in four signal peaks, including for pyridinic-N at ~398.4 eV, pyrrolic-N at ~400.0 eV, graphitic-N at ~401.0 eV, and pyridinic-N-O at ~403.0 eV. The decomposition of pyridinic-N and pyrrolic-N to doped-N sites originated from the amino acids contributing to the increase in the number of active sites by breaking the carbon bonding [24, 25]. In Fig. 5(i-l), the B 1s XPS spectra exhibit three types of B bonding states formed at the edge of the carbon lattice structure. Although this result was not observed for the N-doped C and P@N-doped C samples without an additional B source (Fig. 5i and 5k), the B-doped C and B@P@N-doped C samples were observed (Fig. 5j and l) and indicated BC_3 peaks at ~191.3 eV, BC_2O at

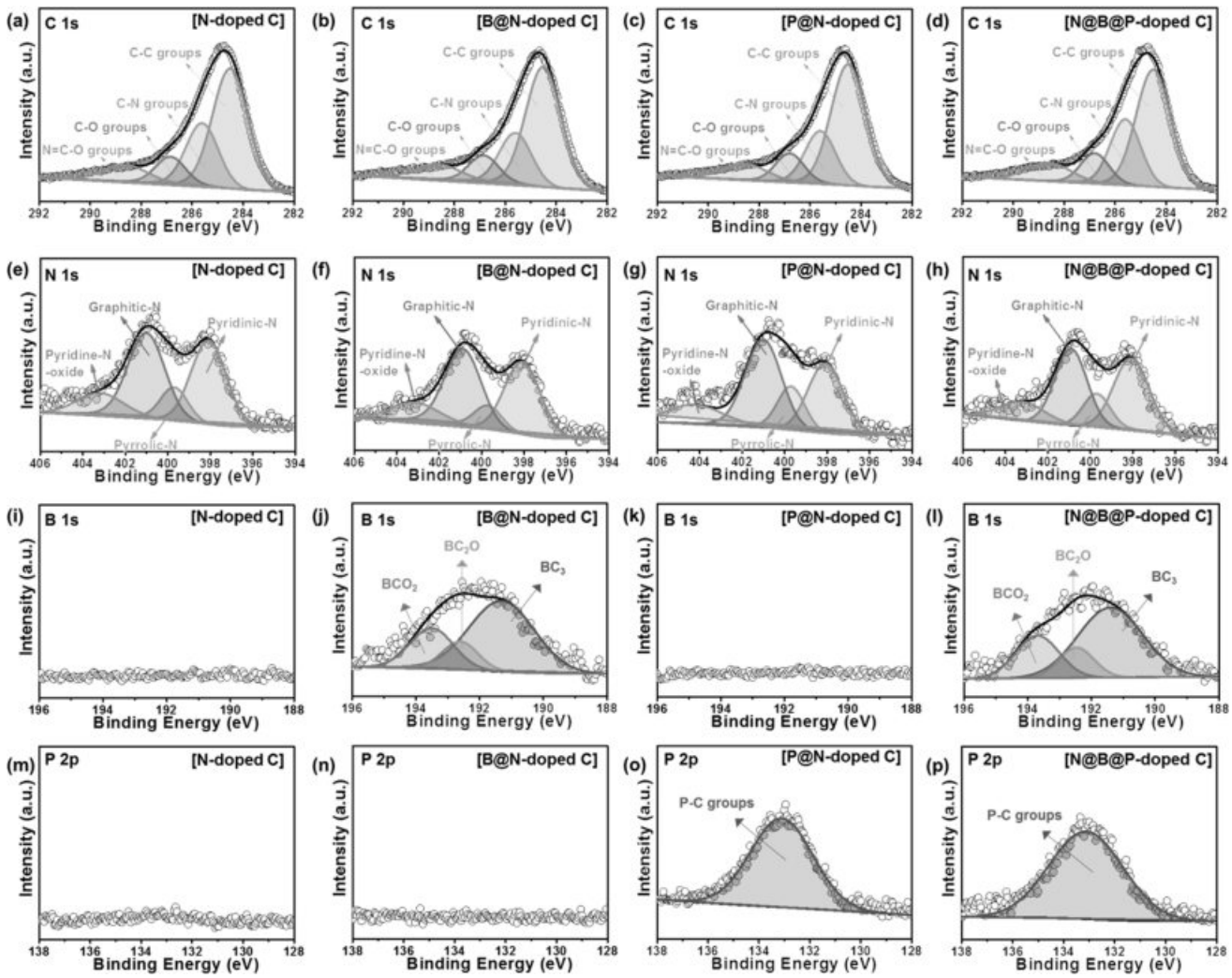

Fig. 5. XPS spectra results of (a–d) C 1s, (e–h) N 1s, (i–l) B 1s, and (m–p) P 2p of N-doped C, B@N-doped C, P@N-doped C, and B@P@N-doped C.

~192.5 eV, and BCO_2 at ~193.8 eV, respectively. The B atoms result in a modified electronic structure that exchanges C atoms and improves electron acceptability [34]. Also, Fig. 5(m–p) shows the P 2p XPS spectrum of the samples. P@N-doped C and N@B@P-doped C show a signal of ~133.0 eV, corresponding to covalent P-C bonding states. This indicates that the doping of P atoms induced by CH_4 cracking at a high temperature above 700 ºC is incorporated into the edge of the graphite layer. In particular, P-C bonding states can be generated at the edge by P doping to produce an O-containing functional group, which leads to improved electrochemical performance due to the increase in wettability [35, 36]. Thus, tunable ternary (B, P, and N)-doped carbon derived from tofu was confirmed by XPS analysis.

Fig. 6(a) shows the cycling performance of N-doped C, B@N-doped C, P@N-doped C, and B@P@N-doped C electrodes at a current density of 100 mA g^{-1} for up to 100 cycles in the potential range of 0.0–3.0 V (vs, Li/Li^+). The specific discharge capacities of the electrodes were 512 mAh g^{-1} for N-doped C, 879 mAh g^{-1} for B@N-doped C, 1070 mAh g^{-1} for P@N-doped C, and 1137 mAh g^{-1} for B@P@N-doped C in the first cycle. These high values are mainly due to the direct formation of a solid electrolyte interface (SEI) layer at the carbon interface, which stores the charge through an interfacial charging. The SEI layer is generally formed during the first cycle due to the reductive decomposition of electrolyte at the electrode surface,

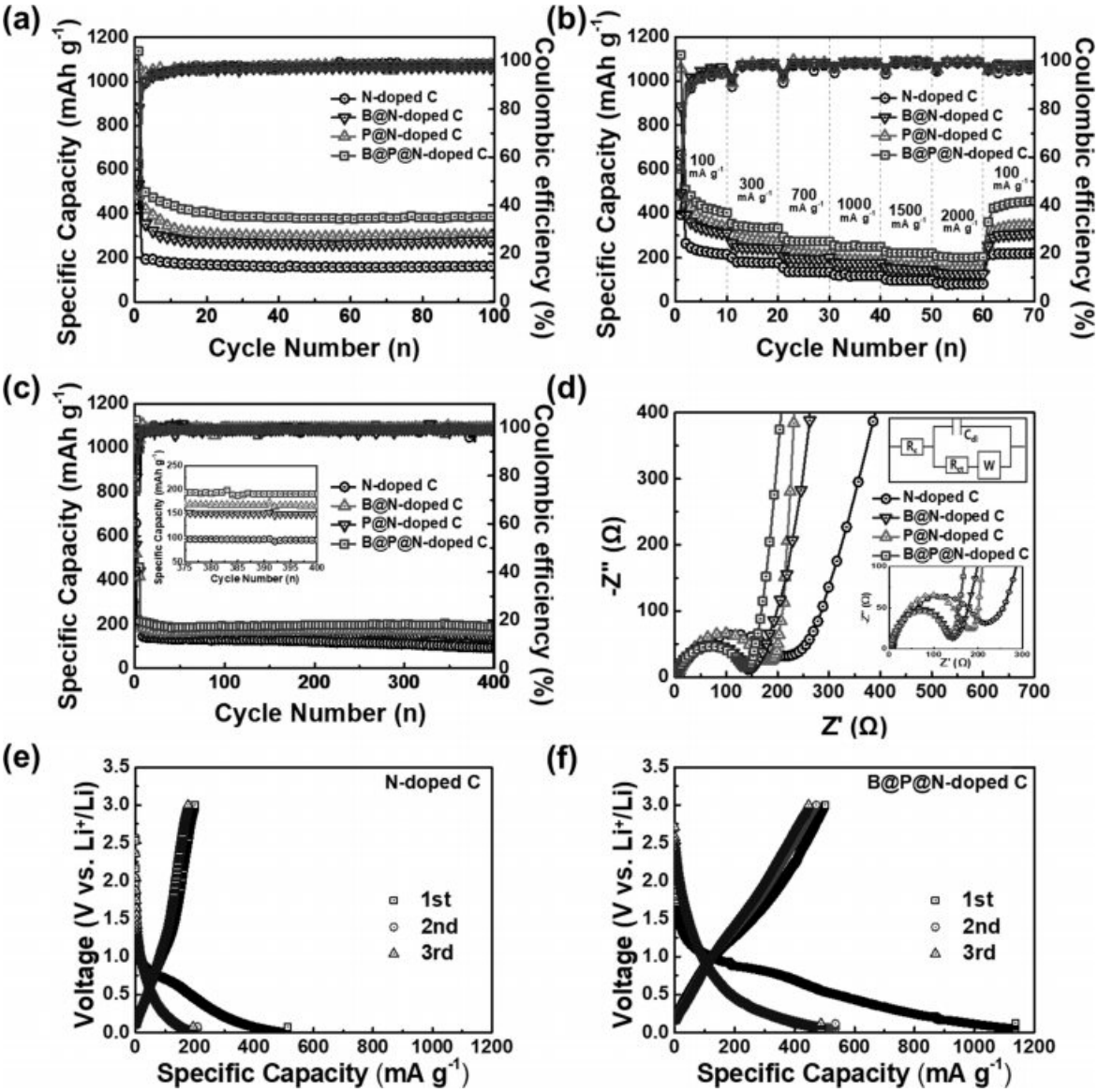

Fig. 6. (a) cycling performance at a current density of 100 mA g^{-1} for up to 100 cycles, (b) Rate-performance at current densities of 100, 300, 700, 1000, 1500, and 2000 mA g^{-1}, (c) high-rate cycling performance at 2000 mA g^{-1} for up to 400 cycles, (d) Nyquist plots in the frequency range of 10^5 to 10^{-2} Hz at an open circuit potential, and Charge-discharge curves of (e) N-doped C and (f) B@P@N-doped C electrodes at the current density of 100 mA g^{-1} in the potential range of 0.05–3.0 V for 1st, 2nd, and 3rd cycles.

resulting in low initial Coulombic efficiency at the first cycle [42]. Nonetheless, B@P@N-doped C showed a highest initial Coulombic efficiency of 57.1% as compared to P@N-doped C (48.6%), B@N-doped C (44.1%) and N-doped C (38.6%). These results indicate that the additional doping sites within the carbon lattice can effectively improve the initial Coulomb efficiency of electrodes due to a low energy barrier for the Li-ion insertion. In addition, all the electrodes reached almost 100% coulombic efficiency after 5 cycles, which suggests the high reversibility. In addition, after the first 100 cycles, the specific discharge capacities of the electrodes were 162 mAh g^{-1} for N-doped C, 279 mAh g^{-1} for B@N-doped C, 303 mAh g^{-1} for P@N-doped C, and 381 mAh g^{-1} for B@P@N-doped C. Except for the N-doped C, the samples exhibited specific capacities superior to that of the commercial graphite electrode (196 mAh g^{-1} after 100 cycles) [37]. In other words, B@N-doped C and P@N-doped C showed higher initial and final specific discharge capacities than N-doped C, which was related to the improved electron mobility from doped B atoms, and the increase in the number of functional groups on the carbon surface by doped P atoms [19, 20, 31]. Furthermore, B@P@N-doped C showed the highest initial and final specific discharge capacities compared with the electrodes fabricated with doped B or P elements because of the synergistic effect of tunable ternary doping in carbon derived from tofu. Fig. 6(b) shows the rate performance obtained at current densities of 100, 300, 700, 1,000, 1,500, and 2,000 mA g^{-1}. All samples exhibit gradually decreasing specific capacities as the current density increases. Also, B atom or P atom doped carbon shows higher specific discharge capacities than N-doped carbon because of the enhanced carbon conductivity from B-doping, and the increase in the number of functional groups on the carbon surface from P-doping. In particular, the B@P@N-doped C electrode shows the highest specific capacities (438, 338, 276, 249, 221, and 202 mAh g^{-1} at current densities of 100, 300, 700, 1000, 1500, and 2000 mA g^{-1}, respectively). Subsequently, when the current density returned to 100 mA g^{-1}, B@P@N-doped C recovered to 435 mAh g^{-1}, which indicated 99% retention of the original specific capacity. This performance improvement is because of the synergistic effect of the enhanced carbon conductivity from the B-doping and increase in the number of functional groups from P-doping, as well as increase in the number of active sites from N-doping. To demonstrate the cycle stability of the electrodes in Fig. 6(c), all electrodes were tested for up to 400 cycles at a high current density of 2000 mA g^{-1}. N-doped C shows only 95 mAh g^{-1} after 400 cycles, which implies low cycle stability compared with the other samples. The specific discharge capacities after 400 cycles were 149 mAh g^{-1} for B@N-doped C, and 166 mAh g^{-1} for P@N-doped C. Furthermore, B@P@N-doped C was observed to have a specific discharge capacity of 190 mAh g^{-1} after 400 cycles at 2,000 mA g^{-1}, indicating the best specific capacity and the best cycle stability among the samples. Fig. 6(d) shows the Nyquist plots of all electrodes in the frequency range of 10^5 to 10^{-2} Hz at an open circuit potential [38]. In the measurement graph, the semicircle in the high-frequency region is ascribed to the charge transfer resistance (R_{ct}) at the anode and electrolyte interface, and the straight line in the low-frequency region is called the Warburg impedance, corresponding to Li ion diffusion at the anode. N-doped C shows the highest R_{ct} and Warburg impedance compared with the other samples. B@N-doped C exhibits improved kinetics in electrode from increased carbon conductivity, implying a fast and stable reaction on the electrode surface due to the increased charge transfer rate [39, 40]. The P@N-doped C showed an ideal vertical slope for Warburg impedance because of the increase in the number of functional groups, which can improve the contact performance between the electrode and the electrolyte [41]. Furthermore, B@P@N-doped C showed significantly increased charge transfer kinetics and functionality compared with other electrodes due to the synergistic effect of B and P doping. For this reason, LIBs fabricated with B@P@N-doped C can exhibit improved specific capacity and high-rate cycling performance. Fig. 6(e, f) shows typical voltage capacity profiles of N-doped C and B@P@N-doped C electrodes at a current density of 100 mA g^{-1} in the potential range of 0.05–3.0 V for 1st, 2nd, and 3rd cycles. During the first discharge process, both electrodes showed a voltage plateau slope under 1.0 V. The flat voltage plateau is considered as a general phenomenon in carbon-based electrodes, which is caused by the formation of the SEI layer and the irreversibility of Li ion insertion into the carbon lattice [43, 44]. The initial discharge and charge capacities are 512.6 mAh g^{-1} and 201.5 mAh g^{-1} for N-doped C, and 1137.8 mAh g^{-1} and 536.4 mAh g^{-1} of B@P@N-doped C, corresponding to the Coulombic efficiency of 39.3% and 44.1%, respectively. These results indicate that the improved energy storage performance of the B@P@N-doped C electrodes are due to the introduction of additional doping sites to decrease energy barriers on Li ion insertion.

Thus, we have demonstrated enhanced lithium storage performance using a designed ternary doping system, which can be provide advantages as follows. Protein-based carbon derived from tofu demonstrated an increased number of active sites on its surface after N-doping in amino acid, which improved the specific discharge capacity. Furthermore, the B and P elements in the B@P@N-doped C provided a fast diffusion path and increased the number of contact sites for Li ions due to enhanced electrical conductivity and the increase in the number of functional groups, thereby greatly improving the high-rate cycling performance. Therefore, B@P@N-doped C derived from tofu could be a potential electrode for high-performance LIBs.

Conclusions

Tunable ternary (B, P, and N) doped carbon was successfully prepared with a sequential doping process and carbonization. The B@P@N-doped C electrode exhibited a high specific discharge capacity (381 mAh g^{-1} at 100 mA g^{-1} after 100 cycles). Moreover, this electrode showed outstanding cycling stability at a high current rate (190 mAh g^{-1} after 400 cycles at 2,000 mA g^{-1}). The superior electrochemical performance can be explained by the following: (i) excellent specific discharge capacities resulted from the increase in active carbon sites due to the N-doped carbon derived from the amino acid in Tofu, and (ii) the outstanding high-rate cycling performance was associated with enhanced carbon conductivity from B-doping and the increase in the number of functional groups on the carbon surface by P-doping. Therefore, tunable ternary-doped carbon may be used as a candidate anode material in the development of high-rate cycling LIBs.

Acknowledgement

This work was supported by the National Research Foundation of Korea (NRF) grant funded by the Korea government (MSIT) (No. 2019R1 A2 C1005836).

References

1. N. A. Kaskhedikar, and J. Maier, Adv. Mater. 21[25-26] (2009) 2664-2680.
2. S. Goriparti, E. Miele, F. D. Angelis, E. D. Fabrizio, R. P Zaccaria, and C. Capiglia, J. Power. Sources 257 (2014) 421-443.
3. M. M. Thackeray, C. Wolverton, and E. D. Isaacs, Energy Environ. Sci. 5 (2012) 7854-7863.
4. I. Mochida, C.-H. Ku, and Y. Korai, Carbon. 39[3] (2001) 399-410.
5. Q. Jiang, Z. Zhang, S. Yin, Z. Guo, S. Wang, and C. Feng, Appl. Surf. Sci. 379 (2016) 73-82.
6. A. Caballero, L. Hernán, and J. Morales, Chem. Sus. Chem. 4[5] (2011) 658-663.
7. H. Xu, H. Zhang, Y. Ouyang, L. Liu, and Y. Wang, Electrochim. Acta 214 (2016) 119-128.
8. L. Wang, J. Xue, B. Gao, P. Gao, C. Mou, and J. Li, RSC Adv. 4 (2014) 64744-64746.
9. P. Zheng, T. Liu, J. Zhang, L. Zhang, Y. Liu, J. Huang, and S. Guo, RSC Adv. 5 (2015) 40737-40741.
10. N. Fechler, S.-A. Wohlgemuth, P. Jäker, and M. Antonietti, J. Mater. Chem. A 1 (2013) 9418-9421.
11. M. Sevilla, A. B. Fuertes, and R. Mokaya, Energy Environ. Sci. 4 (2011) 1400-1410.
12. D.-Y. Lee, G.-H. An, and H.-J. Ahn, J. Ind. Eng. Chem. 52 (2017) 121-127.
13. G.-H. An, H. Kim, and H.-J. Ahn, Appl. Surf. Sci. 463 (2019) 18-26.
14. G.-H. An, H.-G. Jo, and H.-J. Ahn, J. Alloy. Compd. 763 (2018) 250-256.
15. Y.-G. Lee, G.-H. An, and H.-J. Ahn, J. Alloy. Compd. 751 (2018) 62-68.
16. J. P. Paraknowitsch, and A. Thomas, Energy Environ. Sci. 6 (2013) 2839-2855.
17. W. Wang, I. Ruiz, K. Ahmed, H. H. Bay, A. S. George, J. Wang, J. Butler, M. Ozkan, and C. S. Ozkan, Small 10[16] (2014) 3389-3396.
18. J.-Y. Choi, D. J. Lee, Y. M. Lee, Y.-G. Lee, K. M. Kim, J.-K. Park, and K. Y. Cho, Adv. Funct. Mater. 23[17] (2013) 2108-2114.
19. L. G. Bulusheua, A. V. Okotrub, A. G. Kurenya, H. Zhang, H. Zhang, X. Chen, and H. Song, Carbon. 49[12] (2011) 4013-4023.
20. C. Zhang, N. Mahmood, H. Yin, F. Liu, and Y. Hou, Adv. Mater. 25[35] (2013) 4932-4937.
21. Y.-W. Zeng, D.-K. Ma, W. Wang, J.-J. Chen, L. Zhou, Y.-Z. Zheng, K. Yu, and S.-M. Huang, Appl. Surf. Sci. 342 (2015) 136-143.
22. C. Du, H. Huang, Y. Wu, S. Wu, and W. Song, Nanoscale 8 (2016) 16251-16258.
23. Z. Liu, and L. Dai, Nat. Rev. Mater. 1 (2016) 1-12.
24. H. Liu, Y. Zhang, R. Li, X. Sun, S. Désilets, H. A. -Rachid, M. Jaidann, and L.-S. Lussier, Carbon. 48[5] (2010) 1498-1507.
25. T. Sharifi, C. Hu, X. Jia, and T. Wågberg, ACS Nano 6[10] (2012) 8904-8912.
26. C.-P. Yang, Y.-X, Yin, H. Ye, K.-C. Jiang, J. Zhang, and Y.-G. Guo, ACS Appl. Mater. Interfaces 6 (2014) 8789-8795.
27. Z. Zhou, A. Wakamiya, T. Kushida, and S. Yamaguchi, J. Am. Chem. Soc. 134 (2012) 4529-4532.
28. H. Zhang, X. Li, D. Zhang, L. Zhang, M. Kapilashrami, T. Sun, P.-A. Glans, J. Zhu, J. Zhong, Z. Hu, J. Guo, and X. Sun, Carbon. 103 (2016) 480-487.
29. Y. Li, Z. Wang, L. Li, S. Peng, L. Zhang, M. Srinivasan, and S. Ramakrishna, Carbon. 99 (2016) 556-563.
30. J. Zhang, N. Nie, Y. Liu, J. Wang, F. Yu, J. Gu, and W. Li, ACS Appl. Mater. Interfaces 7 (2015) 20134-20143.
31. L. Zhang, G. Xia, Z. Guo, X. Li, D. Sun, and X. Yu, Int. J. Hydrog. Energy 41[32] (2016) 14252-14260.
32. S. Zhao, J. Liu, C. Li, W. Ji, M. Yang, H. Huang, Y. Liu, and Z. Kang, ACS Appl. Mater. Interfaces 6[24] (2014) 22297-22304.
33. J.-H. Zhou, Z.-J. Sui, J. Zhu, P. Li, D. Chen, Y.-C. Dai, and W.-K. Yuan, Carbon. 45[4] (2007) 785-796.
34. C. Wang, Z. Guo, W. Shen, Q. Xu, H. Liu, and Y. Wang, Adv. Funct. Mater. 24[35] (2014) 5511-5521.
35. T. Panja, D. Bhattacharjya, and J.-S. Yu, J. Mater. Chem. A 3 (2015) 18001-18009.
36. X. Ma, G. Ning, C. Qi, C. Xu, and J. Gao, ACS Appl. Mater. Interfaces 6[16] (2014) 14415-14422.
37. G.-H. An, D.-Y. Lee, and H.-J. Ahn, J. Alloy. Compd. 722 (2017) 60-68.
38. G.-H. An, D.-Y. Lee, and H.-J. Ahn, ACS Appl. Mater. Interfaces 9[14] (2017) 12478-12485.
39. Q. Xia, H. Yang, M. Wang, M. Yang, Q. Guo, L. Wan, H. Xia, and Y. Yu, Adv. Energy. Mater. 7[22] (2017) 1701336-1701344.
40. H. Tabassum, R. Zou, A. Mahmood, Z. Liang, Q. Wang, H. Zhang, S. Gao, C. Qu, W. Guo, and S. Guo, Adv. Mater. 30[8] (2018) 1705441-1705447.
41. D.-Y. Shin, K.-W. Sung, and H.-J. Ahn, Appl. Surf. Sci. 478 (2019) 499-504.
42. Y.-T. Park, and K.-T. Lee, J. Ceram. Process. Res. 19[3] (2018) 257-264.
43. J. Ann, S. Choi, J. Do, S. Lim, and D. Shin, J. Ceram. Process. Res. 19[5] (2018) 413-418.
44. G. Ye, X. Zhu, S. Chen, D. Li, Y. Yin, Y. Lu, S. Komarneni, and D. Yang, J. Mater. Chem. A. 5 (2017) 8247-8254.